Defence Technology 23 (2023) 92–99

Contents lists available at ScienceDirect

Defence Technology

journal homepage: www.keaipublishing.com/en/journals/defence-technology

Estimating energy release performance of oxidizer-activated aluminum fuel particles under ultrafast stimulus

Ya-ru Li [a], Hui Ren [a, *], Xin-zhou Wu [a], Hui-xin Wang [a], Xi-long Yu [b]

[a] State Key Laboratory of Explosion Science and Technology, Beijing Institute of Technology, Beijing, 100081, China
[b] State Key Laboratory of High Temperature Gas Dynamics, Institute of Mechanics, Chinese Academy of Sciences, Beijing, 100190, China

ARTICLE INFO

Article history:
Received 1 September 2021
Received in revised form
26 December 2021
Accepted 4 January 2022
Available online 10 January 2022

Keywords:
Aluminum
Glycidyl azide polymer
Laser
Detonation
Explosive
Ultrafast stimulus

ABSTRACT

Aluminum (Al) particles are good fuel additives to improve the energy output performances of explosives. Under detonation environment, reaction delay of Al particles plays a key role in the energy release efficiency. Up to date, reaction delay of Al particles is still limited by the efficiency of mass and heat transfer from oxidizers to Al particles. To address this issue, a homogeneous fuel-oxidizer assembly has recently become a promising strategy. In this work, oxidizer-activated Al fuel particles (ALG) were prepared with glycidyl azide polymer (GAP) as the oxidizer. The ALG was in uniform spherical shape and core-shell structure with shell layer of around 5 nm which was observed by scanning electron microscope and transmission electron microscope. The localized nanoscale mid-IR measurement detected the uniform distribution of characteristic absorption bond of GAP in the shell layer which confirmed the homogenous fuel-oxidizer structure of ALG. A thermal gravimetric analysis of ALG at ultrafast heating rate of 1000 °C/min under argon atmosphere was conducted. The decomposition of GAP finished much earlier than that of GAP at heating rate of 10 °C/min. Under ultrafast high laser fluence, the reaction response of ALG was characterized and compared with that of micro-sized Al (μAl). With the increase of laser energy, the propagation distance of the shock wave increased. However, the velocity histories were nearly the same when energies were lower than 299 mJ or higher than 706 mJ. The propagation distance of the shock wave for ALG was 0.5 mm larger than that for μAl at 2.1 μs. The underwater explosion showed the peak pressure and the shock wave energy of the ALG-based explosive were both higher than those of the μAl-based explosive at 2.5 m. This study shows the feasibility to improve the energy release of Al-based explosives via using the oxidizer-activated Al fuel particles with energetic polymer as the oxidizer.

1. Introduction

Metal fuels have higher energy densities than explosives. When added to explosive composites, metal fuels can significantly enhance their energy output efficiencies and improve their blast effects, which will especially benefit the underwater performances [1–5]. It is known that the detonation process of explosive is at nanosecond timescale during which temperature and pressure jump to thousands of K and tens of GPa, respectively. Under such complex environment, the reaction mechanisms of the metal fuels are far different from their combustion or oxidation mechanisms at slow heating rates [6]. One commonly accepted reaction mechanism for the aluminum (Al) particle under detonation atmosphere is constructed based on Chapman-Jouguet (C-J) model. According to this model, the Al particle cannot participate in the reaction at the C-J plane; and the reaction of Al particle occurs after the expansion of detonation products and causes a long sequential reaction zone [7–9]. Therefore, compared with non-aluminized explosives, aluminized explosives will generate more heat and working capacity, but with sacrifice of detonation velocity and pressure. To improve this situation, the reaction of Al needs to be early enough to participate in the reaction at C-J plane.

* Corresponding author.
E-mail address: renhui@bit.edu.cn (H. Ren).
Peer review under responsibility of China Ordnance Society

https://doi.org/10.1016/j.dt.2022.01.001

Up to date, it is still a big challenge to accelerate the reaction of Al particle, as the efficiency of mass and heat transfer between oxidizers and Al particles is a key obstacle. To shorten the mass and heat diffusion distance, the nano-sized Al particle has become a good alternative over the past few decades. Meanwhile, the bigger surface area of nano-sized Al particle will increase the contact probability with the heat and surrounding products. The aluminized explosives containing nano-sized Al particles show better performances than those containing micro-sized Al particles with respect to combustion velocity, ignition time and duration of maximal explosion pressure [10–13]. However, when engineering Al nanoparticles, they tend to agglomerate together due to high surface energy, which will inhibit the heat and mass diffusion pathway. To address this issue, researchers put the focus on the fabrication of homogeneous fuel-oxidizer composites [14–16]. Compare with physical mixtures, such composites can achieve uniform and intimate contact between fuels and oxidizers, which will significantly enhance synergistic energy release. For example, Al/nitrocellulose mesoparticles based propellants show approximately 35% higher burning rate with identical burning rate exponent than traditional micro-sized particles based propellants [16].

Besides the nitrocellulose (NC), another energetic polymer—glycidyl azide polymer (GAP) [17], has attracted growing attention in improving the energetic performance of system in recent years [18–23]. Lima et al. employed modified-GAP to cap Al via high-energy ball milling technique. Thermal gravimetric and differential thermal analyses indicated that resulted particles exhibited higher reactivity compared with Al particles capped with non-energetic organic layers [18]. In addition to high reactivity, Zeng et al. found GAP grafted Al particles showed enhanced energy performance with preferable heat release rate in the ignition test, and improved water resistance with static water contact angle of 142.4° [19]. Our group also prepared GAP coated Al particles by electrospray technique [24,25]. It was learned that the heat generated by polymer decomposition could accelerate the combustion propagation, and the GAP coated Al particles owned higher combustion propagation rate than the NC coated ones due to the higher energy content of GAP.

Although reaction performance of the Al/GAP system under slow heating rate has been extensively studied, its behavior at fast heating rate like explosive atmosphere is still not well understood, which is crucial for the design of Al/GAP based explosives. In this work, energy release performances of Al/GAP particles under ultrafast impulses were investigated. First, the decomposition behavior of Al/GAP particles under fast heating rate was studied by high speed thermal gravimetric analysis. Second, the laser-induced air shock from energetic materials (LASEM) technique was employed to assess the reaction performance of the Al/GAP particles on the post-detonation timescale. The laser source for LASEM technique is usually of nanoseconds pulse duration with fluence as large as billions of W/cm^2. When applied on materials (energetic or inert), the plasma at tens of thousands kelvin will be excited [26–29]. Therefore, the LASEM technique has recently become an attractive approach to evaluate the energy release of metal powders and mixtures of metal powder and polymer on the detonation and post-detonation timescales [30–32]. In addition, energy release performance of Al/GAP particles under real explosion atmosphere was characterized by underwater explosion experiment. The underwater explosion experiment is a good method to evaluate the energy content of energetic materials, as the water environment can conserve the explosion energy to the maximum extent [33]. From this analysis, the influence of Al/GAP particles on the energy release of explosive composites can be examined.

2. Experiment

2.1. Materials and characterization

Al/GAP particles (ALG) with GAP of 16.7 wt.% were prepared by in-situ strategy in the laboratory, and detailed strategy was provided in the work of Wang [34]. The morphology of ALG was observed by a scanning electron microscope (SEM, Hitachi S4800, Hitachi Ltd., Japan) and a transmission electron microscope (TEM, Tecnai G2 F20, FEI Co., USA). The localized nanoscale mid-IR measurement was carried out using a Nano-IR2 system (AFM-IR, Anasys Instruments, CA, USA) over the range of 900–1500 cm^{-1}. Infrared spectrum was obtained using a VERTEX 70 Fourier Transform infrared spectrometer (FTIR, Bruker, Germany) over the range of 400–4000 cm^{-1}. The thermal gravimetric analyses (TGA) of samples were carried out using a NETZSCH STA 449 F3 thermal analyzer device (NETZSCH, Co., Germany) under 50 mL/min dynamic argon atmosphere. The test under heating rate of 1000 °C/min was conducted in an open platinum crucible. And the tests under heating rate of 10 °C/min were conducted in Al_2O_3 crucibles with pin hole covers. Al particles of 25 μm (μAl, purity: 99.95%) were purchased from Aladdin Chemistry Co., Ltd, as a comparison to ALG in the LASEM and underwater detonation experiments.

2.2. LASEM experiment

A Nd:YAG solid laser (1064 nm, InnoLas Laser, Germany) with 6 ns pulse duration and a laser-beam divergence of $\alpha < 0.5$ mrad was used to stimulate the laboratory explosion atmosphere. The diameter of laser pulse was focused to be 1 mm by a 5.4 cm convex lens with an effective focal length of 500 mm. The estimated uncertainty for laser energy was no more than 1%. The estimated uncertainty in the focused spot diameter was 2%. The laser fluence was determined from the measured pulse energy and the spot diameter; hence a maximum of 2% uncertainty was expected for the fluence value. A flash lamp system (JML-C2, Germany) with pulse duration ranging from 0.5 to 1.2 ms served as background light. In the experiment, a schlieren system with 75 mm lens was used to detect the density change of the air caused by the reaction. A high speed camera (SIMD8, Specialized Imaging Ltd, UK) under configuration of 952,381 fps and duration of 50 ns for each frame was employed to capture the laser-induced shock wave. The system was triggered by a pulse generator (DG535, Stanford Research Systems, Inc., USA) under the precise time delay measured by an oscilloscope (DPO7104, Tektronix, USA). The time jitter for the delay system was within 2 ns. An energy meter (J-50MB-YAG, Coherent, USA) was used to measure the energy output of the laser at each shot. Five different energies were applied to the samples to get a better understanding on their energy release performances. The samples were attached to the mold surface with the help of a dual adhesive tape. Each sample was tested under the same laser energy for three times. The experiment setup is shown in Fig. 1.

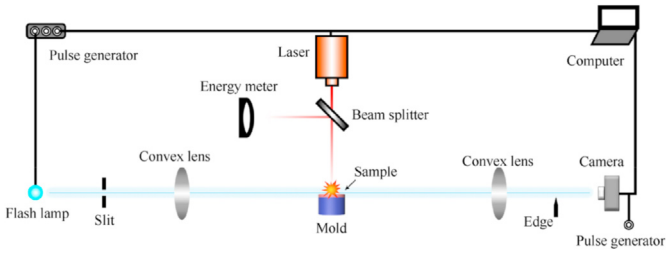

Fig. 1. Diagram for the laser-schlieren system.

2.3. Underwater explosion experiment

The experiment was conducted in an 8.0 × 8.0 m^2 rectangular pool. Samples and sensors were placed in the depth of 4.0 m from the water surface. Two sensors were separately placed in 2.5 m and 3.0 m away from the detonation center. The setup diagram is shown in Fig. 2. Two PCB138A10 underwater blast sensors (measurement range: 68,950 kPa, sensitivity: 0.073 mV/kPa, PCB Group, Inc., USA) were used to measure the shock wave pressure and the period for the bubble's first oscillation generated by the detonation. Samples were all in the shape of cylinder with diameters of 76 mm and weights of 500 g and protected by plastic bags from the water. The main charge was composed of octahydro-1,3,5,7-tetranitro-1,3,5,7-tetrazocine (HMX) and Al, whose detailed information is listed in Table 1. For the initiation process, a 8# industrial detonator served as the initiator followed by 10 g passivated hexahydro-1,3,5-trinitro-1,3,5-triazine (RDX).

3. Results and discussion

3.1. Morphology and chemical composition of ALG

SEM image, TEM image and EDS mapping of N and Al for ALG are presented in Fig. 3(a)-Fig. 3(e). The SEM showed ALG particles were of spherical shape with uniform size distribution mainly around 200 nm. The TEM image showed the layer outside Al particles with a thickness around 5 nm. From the HAADF image, it could be seen the layer outside Al was very thin, which was consistent with the layer in the TEM image. Under the influence of X-ray diffraction, the layer expanded outwards, which caused the EDS mapping area of N spread much larger than the core Al (Fig. 3(d) and Fig. 3 (e)). The azide group was the characteristic group of GAP; hence EDS mapping of N proved the thin layer was GAP. Besides, far-field FTIR spectrum of ALG showed good consistence with that of GAP in Fig. 3(f). Three main characteristic bonds of GAP, i.e. C–O–C (1070 cm^{-1}), C–N (1270 cm^{-1}) and N_3 (2088 cm^{-1}) were all detected in ALG [35–38]. And no new bond was found in the FTIR spectrum of ALG, which suggested that Al and GAP were simply of physical combination. In addition, near-field amplitude image of ALG particle at frequency $\omega = 1070\ cm^{-1}$ was investigated using the Nano-IR2 system to detect the distribution of GAP on the surface of Al. Due to the limitations of the Nano-IR2 measurement range to frequencies ranging from 900 to 1500 cm^{-1}, a frequency $\omega = 1070\ cm^{-1}$ was chosen to identify GAP. The topography of ALG particle in Fig. 3(g) showed the particle size was around 100 nm in height and 220 nm in width. The frequency $\omega = 1070\ cm^{-1}$ was detected over the range of this particle, which indicated the GAP uniformly coated on the surface of Al sphere.

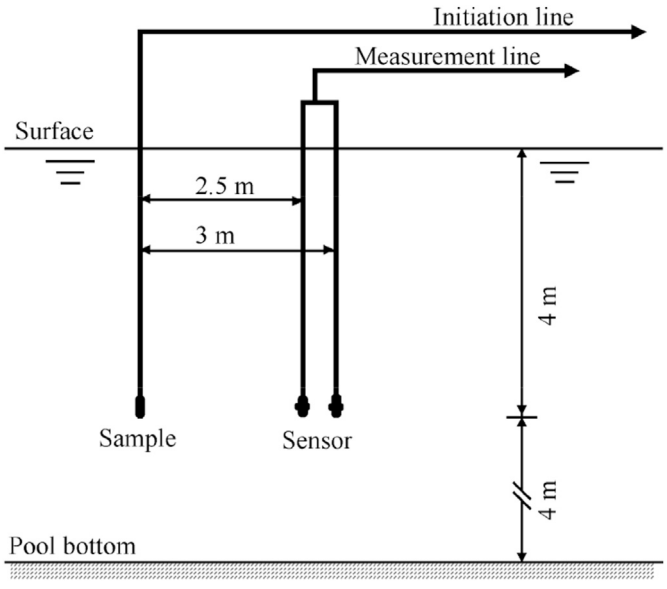

Fig. 2. Diagram for the underwater explosion setup.

Table 1
Information of the test samples.

Formula	HMX	ALG	μAl	Additives
1	62.50	–	33.00	4.5
2	62.50	16.50	16.50	4.5

3.2. Thermal analysis under high speed heating rate

The temperature of a post-detonation area is above 3000 K. An Al particle exposed in such environment will go through ultrafast heating process. According to our previous work [39], the temperature of an Al particle smaller than 1 μm can reach to its melting point (933 K) within 100 ns when the environment temperature is 3500 K. It is important to understand the thermal response of ALG to high heating rate. Therefore, a thermal gravimetric analysis of ALG at heating rate of 1000 °C/min under argon atmosphere was conducted, as shown in Fig. 4(a). As a comparison, thermal gravimetric analyses of ALG and GAP at low heating rate (10 °C/min) under argon atmosphere were also performed, as shown in Fig. 4(a). Corresponding DTG analyses of them are shown in Fig. 4(b).

According to TGA and DTG analyses in Fig. 4, thermal reaction of ALG at heating rate of 1000 °C/min went through two stages. The first stage began at around 174 °C and a fast weight loss of 10% was completed when the temperature reached 204 °C. The second stage finished at 270 °C with a weight loss of 1.5%. In comparison, at heating rate of 10 °C/min, the first stage for thermal reaction of ALG started at nearly the same temperature; however, it did not finish until 274 °C with a weight loss of 5.3%. In addition, its second stage ranged from 274 to 420 °C with a weight loss of about 5.3%. According to Refs. [40–42], the first stage for decomposition of GAP mainly corresponded to the cleavage of N_2 from azide group. The second stage involved the degradation of main chain. The DTG and TGA profiles of GAP in this work showed nearly the same trend to that in work [42]. The DTG curve for ALG at heating rate of 10 °C/min showed two peaks at the same temperature range as GAP. Besides, the total weight loss of GAP in ALG for two stages divided by 16.7% (GAP content in ALG) was basically equal to that of GAP alone. It was also noticed that a slight difference occurred for ALG and GAP at heating rate of 10 °C/min in individual stages of weight loss. For the TGA profile of ALG, the percentage weight loss at the end of first derivative peak was half of the total weight loss in two stages. While for the TGA profile of GAP, the percentage weight loss was more than 57%. This indicated decomposition of GAP was slightly delayed by Al due to their intimate interaction. Case for ALG at 1000 °C/min heating rate was different. The first derivative peak point was nearly −1200%/min, which was 500 times of that for ALG at heating rate of 10 °C/min. In addition to the fast weight loss speed, the weight loss for the former in the first stage was nearly the total weight loss of the latter in two stages. It could be inferred from these results that GAP coating layer would decompose in very short time under high detonation temperature. Owing to the intimate contact between GAP and Al, the interaction between decomposition products of GAP and Al could greatly facilitate the oxidation of Al and hence accelerate the energy release.

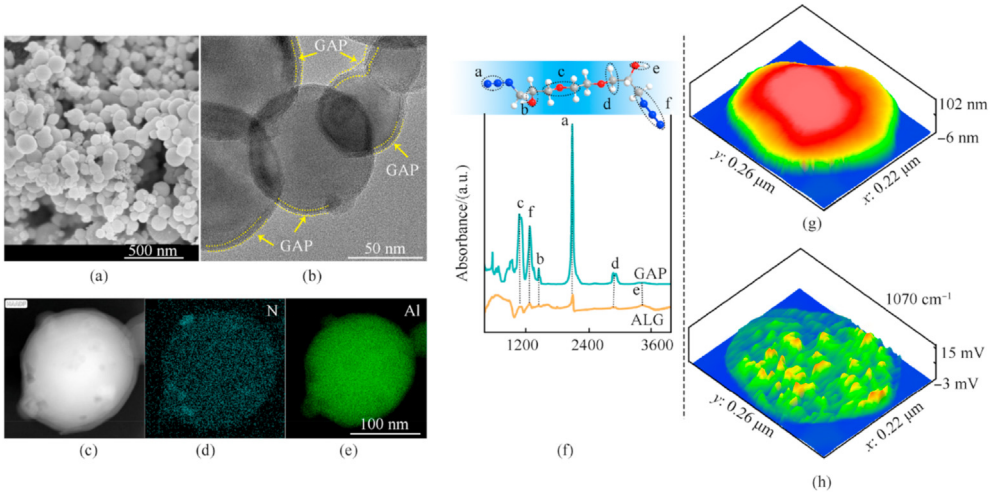

Fig. 3. (a) SEM image; (b) TEM image; (c) HAADF image and (d) corresponding EDS mapping of N and (e) Al for ALG particles; (f) Far-field FTIR spectra of ALG and raw GAP; (g) Topography and (h) near-field amplitude image of ALG particle at frequency $\omega = 1070\ \mathrm{cm}^{-1}$.

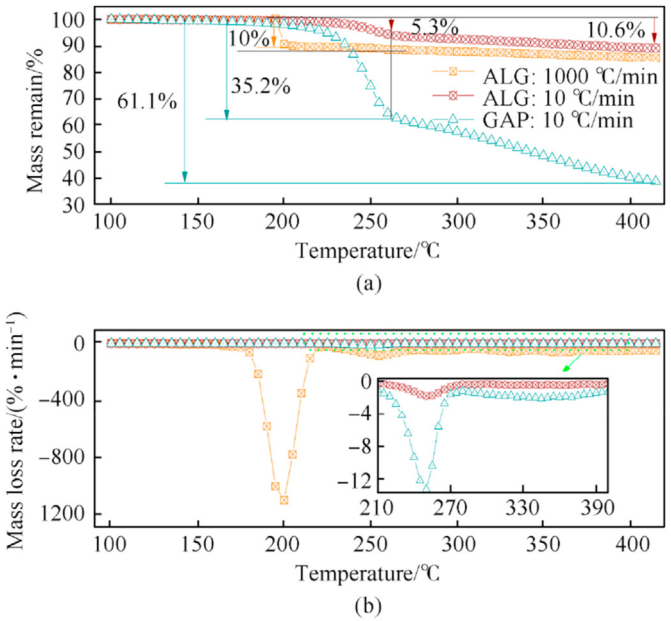

Fig. 4. (a) Non-isothermal TGA of ALG at heating rate of 1000 °C/min, and TGA analyses of ALG and GAP at heating rate of 10 °C/min; (b) Corresponding DTG analysis of ALG at heating rate of 1000 °C/min, and DTG analysis of ALG and GAP at heating rate of 10 °C/min.

3.3. Energy release performance under high laser fluence

Sequences of schlieren images illustrating the post-interaction phenomena initiated by focusing a nanosecond laser pulse on ALG sample under a fluence of 128 J/cm^2 are shown in Fig. 5(a). In the first snapshot, ALG sample produced largest amount of plasma by absorbing laser energy. In the following three snapshots, irradiation of plasma gradually attenuated while a supersonic shock wave emerged and propagated forward. This was because the expansion of plasma pushed the surrounding air forming the shock wave, which would consume lots of plasma energy [43]. According to the blast wave theory [44], the energy consumption (i.e. energy content of the shock wave) in this case was around 774 mJ. It became more evident in the enlarged image of the fifth snapshot that there was an absorbing layer between plasma layer near the sample surface and the shock wave front. This absorbing layer supported the propagation of the shock wave by absorbing the plasma energy [45]. In the beginning, absorbing layer was right behind the shock wave front till 4.15 μs. With time increasing to 6.20 μs, the absorbing layer became separated from the shock wave front. By analyzing the propagation process of the shock wave (red), the absorbing layer front (black) and back (blue) after 6.2 μs, it was found that with increasing time, the shock wave front gradually propagated forward while the absorbing layer front remained stationary, which led to increased distance between them from 25.4 to 61.8 mm, as shown in Fig. 5(b). Meanwhile, the absorbing layer back moved forward causing much thinner absorbing layer. These were caused by the lack of continuous energy supply, as only one laser shot supplied to sample at each test. The sample absorbed the energy and ionized. Ionized sample was able to heat surrounding air and create new ionized layer (absorbing layer), which supported the propagation of the shock wave. After 6.2 μs, the shock wave front separated from the absorbing layer because plasma energy was no longer able to support it.

3.4. Effect of incident laser energy on the shock wave propagation

The propagation of the shock wave greatly depends on the incident laser energy. In this section, laser energies of 213, 299, 406, 706 mJ and 1007 mJ were chosen to investigate the relationship between the incident energy and the shock wave propagation. Propagation profiles of the wave fronts for ALG under different laser energies are shown in Fig. 6(a). The results were fitted based on theory of McKay and Nanai et al. [46,47], as shown in Fig. 6(a). Fitting parameters are listed in Table 2. According to the theory, the propagation distance of the shock wave front (s) grows exponentially over time (t), and their relationship is expressed in Eq. (1). The correlation coefficients for five fitting lines were all more than 0.999, indicating the propagation histories in this work were consistent with the theory. Furthermore, the shock wave front velocity $u(t)$ could be acquired by differentiating $s(t)$ with respect to t, as in Eq. (2). The propagation velocities of wave fronts for ALG under different laser energies are shown in Fig. 6(b).

$$s(t) = s_0 + at^b \tag{1}$$

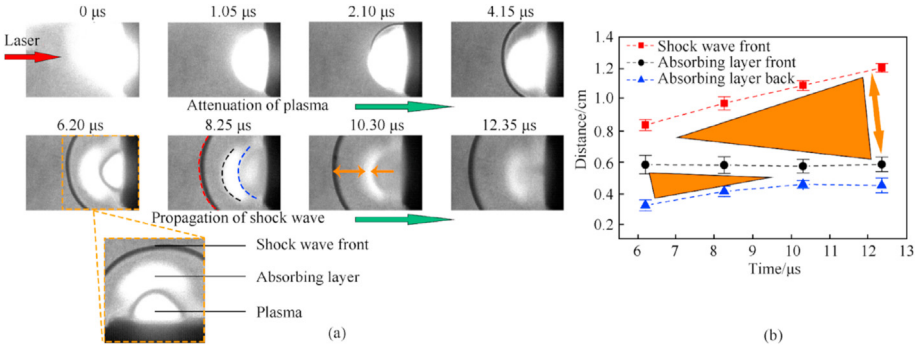

Fig. 5. (a) Sequences of schlieren images obtained after the irradiation of the ALG sample with a 6 ns laser pulse and 1007 mJ energy, 1 mm spot; (b) Distance from the sample surface for the shock wave front, the absorbing layer front and back.

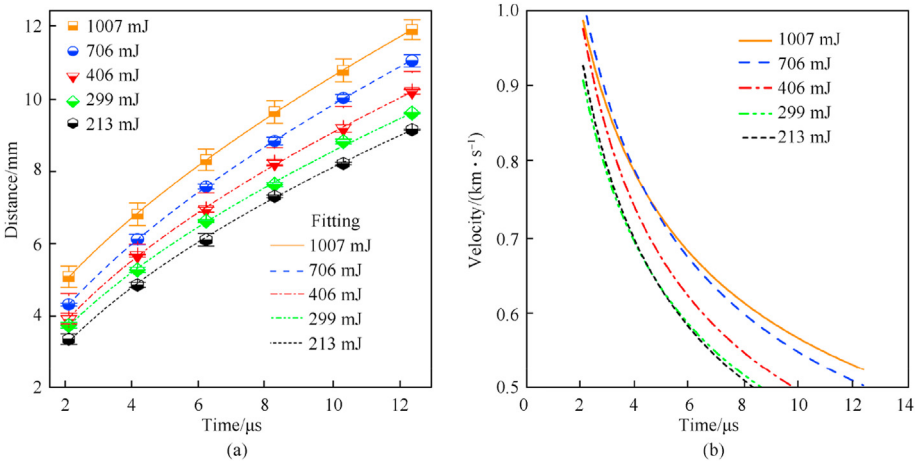

Fig. 6. (a) Propagation profiles and (b) propagation velocities of the shock wave fronts for ALG under different laser energies.

Table 2
Fitting parameters for the shock wave fronts under different energy.

Energy/mJ	s_0	a	b	R^2
1007	1.87	1.99	0.64	0.99990
706	0.80	2.25	0.60	0.99998
406	0.35	2.37	0.57	0.99928
299	0.45	2.14	0.58	0.99911
213	−0.21	2.33	0.55	0.99925

$$u(t) = abt^{b-1} \tag{2}$$

In the equation, b is the attenuation exponent; s_0 and a are the parameters to be determined.

With the increase of laser energy, the propagation distance of the shock wave increased. Under laser energy of 213 mJ, the shock wave only travelled 3.30 mm in 2.1 μs. For the same time range, the shock wave could travel 5.09 mm for laser energy of 1007 mJ. With longer time range, the travel distance would be more significant. This difference could reach to 2.77 mm when the shock wave travelled for 12.35 μs. For the case with laser energies of 706 mJ and 1007 mJ, the difference for travel distances of the shock waves nearly kept the same, so did the case with laser energies of 213 mJ and 299 mJ. Comparing the travel difference between two energy sets of 706 mJ and 1007 mJ, 406 mJ and 706 mJ, it was found that although their energy difference were both 300 mJ, the distance difference for the latter gradually increased. This indicated the propagation of the shock wave was not linearly proportion to laser energy. Particularly, the distance differences both kept increasing for 406 mJ and 299 mJ, 706 mJ and 406 mJ. The increase rate for the former case was much larger than that for the latter case despite their reverse energy differences. For the former case, the distance difference in the end was 1.63 times as much as that in the beginning while this value was 1.38 times for the latter case.

The velocities for energy cases of 1007 mJ and 406 mJ were 985 m/s and 974 m/s at 2.1 μs, respectively. The velocity difference for them was only 11 m/s although their energy difference was 600 mJ. However, velocity difference for energy cases of 406 mJ and 299 mJ was as big as 49 m/s at 2.1 μs while their energy difference was only 107 mJ. Besides, velocity profiles for energy cases of 299 mJ and 213 mJ were nearly the same, so were the cases of 1007 mJ and 706 mJ. The velocity profiles complied with the evolving trends of the propagation distances. Based on the above analyses, it could be concluded that energy increased from 299 mJ to 706 mJ would significantly influence the shock wave velocity in the time range of 2.1 μs–12.35 μs. This situation was caused by the following reasons. The laser energy induced plasma was generated at nanosecond-timescale. The reaction of ALG initiated at microsecond-timescale. The shock wave was born from plasma at nanosecond-timescale, hence the plasma energy could transit to the shock wave at high speed at nanosecond-timescale and the heat loss could be neglected. And with the increase of laser energy, the amount of plasma increased. Besides, the energy deposited in the shock wave increased with the increase of incident laser energy [48]. Therefore, the travel distance of the shock wave at 1.05 μs increased with the laser energy. After 1.05 μs, the propagation of

the shock wave also depended on the reaction energy from the ALG. And the heat loss could not be neglected. Hence the energy deposition and reaction energy for the shock waves at laser energy of 213 mJ and 299 mJ was close to each other. The velocities of their shock waves decreased at the same rate due to the heat loss. Furthermore, the energy deposited in the shock wave increased with the increase of incident energy from 299 to 706 mJ, which led to the growth of temperature behind the shock wave. And the reaction of ALG was promoted due to the temperature growth, which resulted in more reaction heat generation. The heat generated by the reaction could compensate the heat loss to the surroundings to a certain extent. Hence, the velocity of the shock wave kept increasing from 299 to 706 mJ. With the increase of laser energy to 706 mJ, the deposition energy and reaction energy increased to their upper limit. Therefore, the propagation velocity of the shock wave at laser energy of 1007 mJ showed the same behavior to that of 706 mJ.

As a comparison, propagation behavior of μAl under the laser energy of 1007 mJ was also investigated. And the results are shown in Fig. 7. The propagation history of the shock wave front for μAl grew exponentially over time with the exponent of 0.6385. Under the same experiment condition, the propagation distance of ALG wave front was farther than that of μAl wave front. And this difference grew over time from 0.5 to 0.67 mm. The velocity of μAl wave front was comparable to that of ALG. However, with the increase of time, the velocity for the former case dropped faster than the latter case. The performance of ALG was better than that of μAl under such high laser fluence was because heat release from GAP decomposition also supported the propagation of the shock wave in addition to the laser energy.

3.5. Underwater explosion

The pressure profiles for μAl and ALG based explosive formula at distance of 2.5 m are shown in Fig. 8 and Fig. 9. The maximum pressures for them were 14.4 MPa and 15.3 MPa, respectively. This was because ALG could participate in the detonation reaction much earlier than μAl, which would contribute more energy to the C-J plane. After the detonation of the explosive composite, the shock wave overpressure reached to its peak value in no time and soon attenuated to hydrostatic pressure. According to previous study [49], the attenuation process followed exponential form as Eq. (3)

$$p(t) = p_m \cdot \exp(-t/\theta) \tag{3}$$

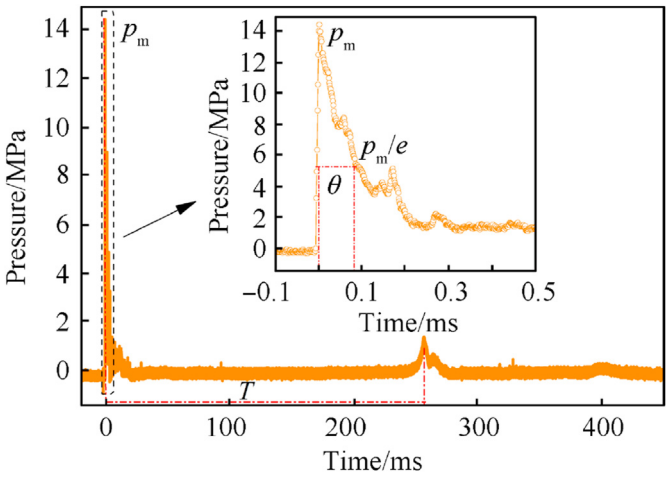

Fig. 8. Pressure profile for μAl-based explosive composite at distance of 2.5 m.

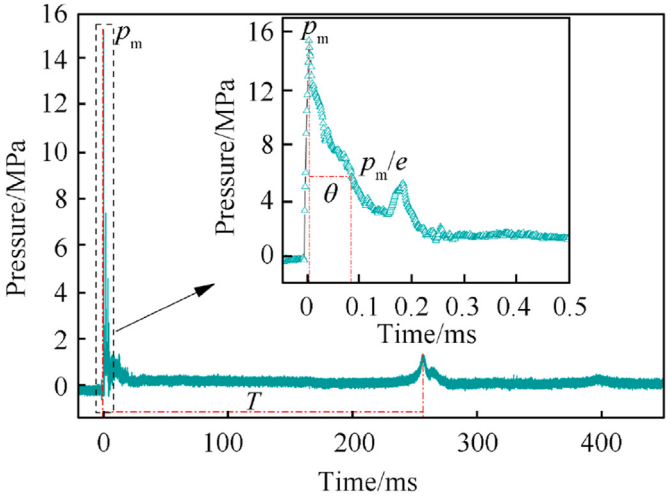

Fig. 9. Pressure profile for ALG-based explosive composite at distance of 2.5 m.

In the equation, $p(t)$ is the shock wave overpressure as a function of time, MPa; p_m is the peak value of the shock wave overpressure, MPa; θ is a time attenuation constant which represents the time

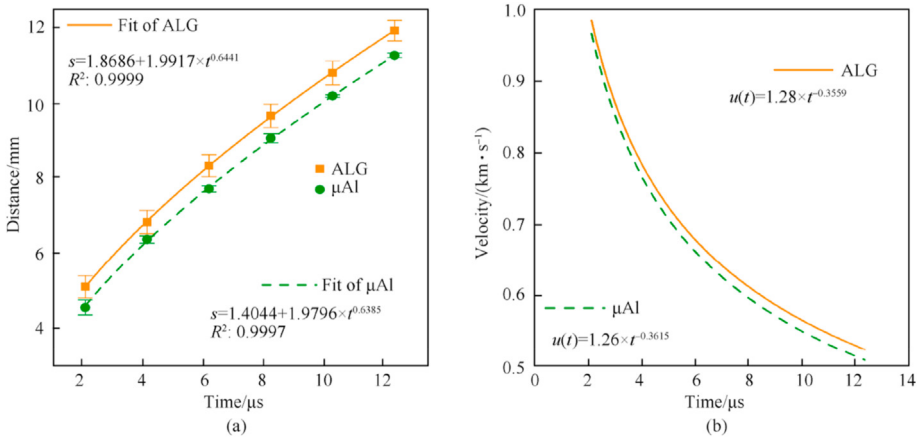

Fig. 7. (a) Propagation profiles of the wave fronts for ALG and μAl under laser energy of 1007 mJ and their corresponding fitting lines; (b) Shock wave front velocity profiles of the wave fronts for ALG and μAl under laser energy of 1007 mJ.

range of the shock wave overpressure attenuates from p_m to p_m/e. In this case, θ were separately 84 μs and 82 μs for μAl-based and ALG-based explosive composites.

Effective shock wave energy generated by unit weight of explosive formula can be expressed by Eq. (4) as below:

$$E_s = \frac{4\pi R^2}{w\rho_0 c_0} \int_0^{6.7\theta} p^2(t)\mathrm{d}t \tag{4}$$

In the equation, R is the distance away from detonation center, m; w is the loading of explosive, kg; ρ_0 is the density of water, kg/m^3; c_0 is the sound velocity of water, m/s.

Bubble energy E_b is the energy carried by detonation product when propagates outwards, which is mainly used to characterize the static effect of energy. It can be calculated based on the work done in expanding the bubble to its first maximum against the hydrostatic pressure [50], as shown in Eq. (5):

$$E_b = \frac{0.675 p_0^{0.4}}{w\rho_0^{1.5}} * T^3 \tag{5}$$

here, p_0 is the static water pressure in the detonation center, Pa; T is the period for the bubble's first oscillation, s. In this case, T was 255.9 ms for μAl-based explosive composite and 255.6 ms for ALG-based explosive composite.

The total energy for underwater explosion should be the addition of effective shock wave energy and bubble energy (Eq. 6), neglecting the energy loss in the propagation process.

$$E_u = E_s + E_b \tag{6}$$

in the equation, E_u is the total energy, J/kg; E_s is the effective shock wave energy, J/kg; E_b is the bubble energy, J/kg.

Based on the above theories, the shock wave energy, bubble energy and the total energy were calculated. And the results are shown in Fig. 10. Shock wave energy, bubble energy of ALG-based explosive formula at 2.5 m was 0.2 times, 0.1 times of TNT equivalence larger than that of μAl-based explosive formula, respectively. ALG-based explosive formula owned higher shock wave energy

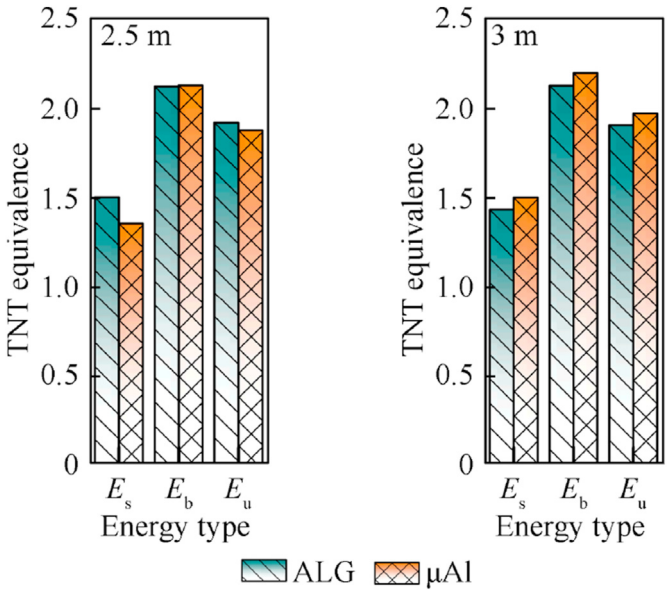

Fig. 10. Energy results for ALG and μAl based explosive composites at different distances.

was because ALG reacted faster than μAl, which would benefit the early reaction of explosive and contribute more energy for the shock wave energy. Bubble energy of ALG-based explosive formula at 2.5 m was slightly lower than that of μAl-based explosive formula, because reaction of μAl lasted longer than ALG, which resulted in a larger T for μAl-based explosive formula. In the distance of 3 m, shock wave energy, bubble energy and total energy of ALG-based explosive formula were all lower than that of μAl-based explosive formula. This was because the reaction of ALG was faster than that of μAl, which led to stronger shock wave intensity; and the stronger intensity of shock wave led to more heat loss with the increase of distance. This indicated that ALG-based explosive formula would show better performance in near field underwater explosion.

4. Conclusions

(1) The morphology of ALG was characterized by SEM and TEM. The results revealed that homogenous oxidizer-fuel structure was fabricated. And the constitution state of ALG was observed by nano-IR and FTIR spectrum. It showed that GAP was uniformly distributed outside the Al sphere.

(2) The reaction of ALG at ultrafast heat stimulus was characterized. Under heating rate of 1000 °C/min, the decomposition of GAP went through two stages. The first stage finished much earlier than that of GAP under 10 °C/min. In addition, the weight loss for the first stage was 10%, which accounted for nearly 87% of the total weight loss. It could be concluded that with ultrafast heating stimulus, the reaction of GAP could be greatly accelerated, which would benefit its activation to Al under detonation environment.

(3) The reaction of ALG at ultrafast laser stimulus was examined. Under laser energy of 1007 mJ, the absorbing layer was not distant from the shock wave front until 6.2 μs. Besides, with increasing time, the distance between the shock wave front and the absorbing layer gradually increased from 25.4 to 61.8 mm. In addition, the propagation distance of the shock wave grew with the increase of laser energy from 213 to 1007 mJ. Under the same laser energy stimulus, the shock wave velocity and propagation distance of ALG were much faster and larger than those of μAl, which showed the advantage of ALG in dealing with ultrafast stimulus.

(4) An underwater explosion experiment was conducted to estimate the behavior of ALG in underwater explosive applications. The peak pressure and the shock wave energy of ALG-based explosive were both higher than those of μAl-based explosive in 2.5 m, indicating reaction rate of ALG was faster than that of μAl. This study provided the possibility to significantly improve the energy output performances of Al-based explosives through energetic polymer activated Al fuel particles.

Since the interaction of GAP and Al under ultrafast stimulus is necessary for understanding the energy release behavior of ALG in detonation environment. As an optimum approach to understand this complex process, a combination of molecular dynamic simulation and improved experimental work will be the focus of following studies.

Declaration of competing interest

The authors declare that they have no known competing financial interests or personal relationships that could have appeared to influence the work reported in this paper.

Acknowledgements

The authors would like to acknowledge National Natural Science Foundation of China (Grant No. 11832006, U1530262, 21975024).

References

[1] Ye MQ, Zhang ST, Liu SS, Han AJ, Chen X. Preparation and characterization of pyrotechnics binder–coated nano-aluminum composite particles. J Energetic Mater 2016;35(3):300–13.
[2] Kappagantula KS, Pantoya ML, Horn J. Effect of surface coatings on aluminum fuel particles toward nanocomposite combustion. Surf Coating Technol 2013;237(237):456–9.
[3] Liu DY, Zhao P, Chan SHY, Hng HH, Chen L. Effects of nano-sized aluminum on detonation characteristics and metal acceleration for RDX-based aluminized explosive. Def. Technol. 2021;17(2):327–37.
[4] Jiang F, Wang XF, Huang YF, et al. Effect of particle gradation of aluminum on the explosion field pressure and temperature of RDX-based explosives in vacuum and air atmosphere. Def. Technol. 2019;15(6):844–52.
[5] Elbasuney S, Zaky MG, Bennaya M, Abdelkhalek SM. The potentials of aluminium nanoparticles: novel high energy density material for underwater explosions. IOP Conf Ser Mater Sci Eng 2020;975.
[6] Wang S, Yang Y, Yu H, Dlott D. Dynamical Effects of the oxide layer in aluminum nanoenergetic materials. Propellants, Explos Pyrotech 2010;30(2):148–55.
[7] Xue Z, Xu G, Wang T, Liu Y. By use of KHT equation of state to calculate detonation parameters of explosives. Explos Shock Waves 1998;18:172–6. 02.
[8] Cook MA, Filler AS, Keyes RT, Partridge WS, Ursenbach W. Aluminized explosives. J Phys Chem 1957;61(2):189–96.
[9] Strømsøe E, Eriksen S. Performance of high explosives in underwater applications. Part 2: aluminized explosives. Propellants, Explos Pyrotech 1990;15(2):52–3.
[10] Delisio JB, Hu X, Wu T, Egan GC, Young G, Zachariah MR. Probing the reaction mechanism of aluminum/poly (vinylidene fluoride) composites. J Phys Chem B 2016;120(24):5534–42.
[11] Zhigach A, Leipunskii I, Pivkina A, Muravyev N, Monogarov K, Kuskov M, et al. Aluminum/HMX nanocomposites: synthesis, microstructure, and combustion. Combust Explo Shock+. 2015;51(1):100–6.
[12] Liu D, Chen L, Wang C, Wu J. Aluminum acceleration and reaction characteristics for aluminized CL-20-based mixed explosives. Propellants, Explos Pyrotech 2018;43(6):543–51.
[13] Zhang C, Lin BQ, Li WX, Zhai C, Zhu CJ. Comparative experimental study on explosion characteristics of nano-aluminum powder and common aluminum powder in the explosive device of a long pipeline. Adv Mater Res 2012;341–342:113–8.
[14] Wang J, Qiao Z, Yang Y, et al. Core-shell Al-polytetrafluoroethylene (PTFE) configurations to enhance reaction kinetics and energy performance for nanoenergetic materials. Chem Eur J 2016;22(1):279–84.
[15] Wang J, Qu Y, Gong F, et al. A promising strategy to obtain high energy output and combustion properties by self-activation of nano-Al. Combust Flame 2019;204:220–6.
[16] Young G, Wang H, Zachariah MR. Application of nano-aluminum/nitrocellulose mesoparticles in composite solid rocket propellants. Propellants, Explos Pyrotech 2015;40(3):413–8.
[17] Kubota N, Sonobe T. Combustion mechanism of azide polymer. Propellants, Explos Pyrotech 1988;13(6):172–7.
[18] Lima RJP, Dubois C, Stowe R, Ringuette S. Enhanced reactivity of aluminum powders by capping with a modified glycidyl azide polymer. Int J Energ Mater Chem Propuls 2016;15(6):481–500.
[19] Zeng C, Wang J, He G, Huang C, Yang Z, Liu S, et al. Enhanced water resistance and energy performance of core–shell aluminum nanoparticles via in situ grafting of energetic glycidyl azide polymer. J Mater Sci 2018;53(17):12091–102.
[20] Diaz E, Brousseau P, Ampleman G, Prud'Homme R. Polymer nanocomposites from energetic thermoplastic elastomers and Alex. Propellants, Explos Pyrotech 2003;28(4):210–5.
[21] Eroglu MS, Bostan MS. GAP pre-polymer, as an energetic binder and high performance additive for propellants and explosives: a review. Org Commun 2017;10(3):135–43.
[22] Hussein AK, Zeman S, Elbeih A. Thermo-analytical study of glycidyl azide polymer and its effect on different cyclic nitramines. Thermochim Acta 2018;660:110–23.
[23] Shin WG, Han D, Park Y, Hyun HS, Sung HG, Sohn Y. Combustion of boron particles coated with an energetic polymer material. Kor J Chem Eng 2016;33(10):3016–20.
[24] Yan T, Sun Y, Ren H, Jiao Q. The role of polymers in nano-aluminum@ polymer microspheres fabricated by electrospray. In: 2018 AIAA/ASCE/AHS/ASC: structures, structural dynamics, and materials conference; 2018.
[25] Yan T, Ren H, Li Y, Wang H, Jiao Q. Tailoring structural energetics for enhanced reactivity of nano-aluminum particles based microspheres. Adv Eng Mater 2019;21(8):1900176.
[26] Yudasaka M, Kokai F, Takahashi K, Yamada R, Sensui N, Ichihashi T, et al. Formation of single-wall carbon nanotubes:comparison of CO2 ıaser ablation and Nd :YAGlaser ablation. J Phys Chem B 1999;103(18):3576–81.
[27] Jackson MJ, O'Neill W. Laser micro-drilling of tool steel using Nd:YAG lasers. J Mater Process Technol 2003;142(2):517–25.
[28] Torrisi L, Gammino S, Picciotto A, Margarone D, Laska L, Krasa J, et al. Temperature measurements in plasmas produced by high-power lasers interacting with solid targets. Rev Sci Instrum 2006;77(3):03B708.
[29] Wainwright ER, Dean SW, Lakshman SV. Evaluating compositional effects on the laser-induced combustion and shock velocities of Al/Zr-based composite fuels. Combust Flame 2020;213:357–68.
[30] Gottfried JL. Laboratory-scale method for estimating explosive performance from laser-induced shock waves. Propellants, Explos Pyrotech 2015;40(5):674–81.
[31] Gottfried JL, Klapötke TM, Witkowski TG. Estimated detonation velocities for TKX-50, MAD-X1, BDNAPM, BTNPM, TKX-55, and DAAF using the laser-induced air shock from energetic materials technique. Propellants, Explos Pyrotech 2017;42(4):353–9.
[32] Gottfried JL. Influence of exothermic chemical reactions on laser-induced shock waves. Phys Chem Chem Phys 2014;16(39):21452–66.
[33] Hu H, Chen L, Yan J, Feng H, Song P. Effect of aluminum powder on underwater explosion performance of CL-20 based explosives. Propellants, Explos Pyrotech 2019;44(7):837–43.
[34] Wang H, Ren H, Yan T, Li Y. Micro-structure and active aluminum content of aluminum powder in situ coated by polyvinyl alcohol. Acta Armamentarii 2019;40(7):1373–80.
[35] Wu Y, Zhen G. Properties and application of a novel type of glycidyl azide polymer (GAP)-modified nitrocellulose powders. Propellants, Explos Pyrotech 2015;40(1):67–73.
[36] Basiuk VA, Navarro-González R, et al. PM3, AM1, MNDO and MINDO3 semi-empirical IR spectra simulations for compounds of interest for Titan's chemistry: diazomethane, methyl azide, methyl isocyanide, diacetylene and triacetylene. Spectrochim Acta, Part A 2001;57(3):505–11.
[37] Leppinen JO, Basilio CI, Yoon RH. FTIR study of thionocarbamate adsorption on sulfide minerals. Colloid Surface 1988;32:113–25.
[38] Alvarez R, Cutın E, Romano R, Mack HG, Della Védova C. Spectroscopic studies of trifluoromethanesulfonyl azide, $CF_3SO_2N_3$. Spectrochim Acta, Part A 1998;54(4):605–15.
[39] Li Y, Ren H, Yan T, Jiao Q, Wang H. Reactivity of fluororubber-modified aluminum in terms of heat transfer effect. J Therm Anal Calorim 2020;142(2):871–6.
[40] Korobeinichev OP, Kuibida LV, Volkov EN, et al. Mass spectrometric study of combustion and thermal decomposition of GAP. Combust Flame 2002;129(1–2):136–50.
[41] Fazlıoğlu H, Hacaloğlu J. Thermal decomposition of glycidyl azide polymer by direct insertion probe mass spectrometry. J Anal Appl Pyrol 2002;63(2):327–38.
[42] Eroğlu MS, Güven O. Thermal decomposition of poly(glycidyl azide) as studied by high-temperature FTIR and thermogravimetry. J Appl Polym Sci 1996;61(2):201–6.
[43] Palanco S, Marino S, Gabás M, Bijani S, Ayala L, Ramos-Barrado JR. Particle formation and plasma radiative losses during laser ablation suitability of the Sedov-Taylor scaling. Opt Express 2014;22(13):16552–7.
[44] Jeong SH, Greif R, Russo RE. Shock wave and material vapour plume propagation during excimer laser ablation of aluminium samples. J Phys D: Appl Phys 1999;32(19):2578–85.
[45] Maher WE, Hall RB, Johnson RR. Experimental study of ignition and propagation of laser-supported detonation waves. J Appl Phys 1974;45(5):2138–45.
[46] McKay JA, Bleach RD, Nagel DJ, Schriempf JT. Pulsed-CO_2-laser interaction with aluminum in air: thermal response and plasma characteristics. J Appl Phys 1979;50(5):3231–40.
[47] Nánai L, Hevesi I. Time-resolved spectral investigations of laser light induced microplasma. Spectrochim Acta 1992;48(1):19–24.
[48] Callies G, Berger P, Hugel H. Time-resolved observation of gas-dynamic discontinuities arising during excimer laser ablation and their interpretation. J Phys D Appl Phys 1995;28(4):794–806.
[49] Cole RH. Underwater explosions. Princeton, New Jersey: Princeton Univ. Press; 1948. p. 67–76.
[50] Bjarnholt G. Suggestions on standards for measurement and data evaluation in the underwater explosion test. Propellants, Explos Pyrotech 1980;5(2–3):67–74.